Chapter 8
Geospatial Assessment of Turbidity Along the Ganga River

N. R. Shankar Ram, Anshuman Bhatt, V. M. Chowdary, Khushboo Mirza, Chandra Shekhar Jha, and Chiranjivi Jayaram

Abstract The Ganga River basin is a lifeline to the millions inhabiting the Indian subcontinent. Pollution and deteriorating water quality in this ecosystem have been linked to various anthropogenic activities such as habitation, industrialization, agriculture, etc. The estimation and evaluation of water quality levels are essential for societal and economic development. In recent times, satellite imaging approach is widely used in diverse environmental applications, including water quality monitoring. Turbidity is an indicator of water transparency that is associated with total suspended sediment concentration and other impurities in the water through the process of light attenuation. The present study envisaged surface reflectance values to estimate the water turbidity across the Ganga River system, which is spatially classified into four different river sections. The Modified Normalized Difference Water Index (MNDWI) was used to delineate water pixels from the multispectral satellite datasets, while the turbidity was assessed spatially for different river sections using widely used Turbidity retrieval algorithms. The relative consistency among the selected algorithms was evaluated using collocated *in-situ* measurements during the period 2013–2016. Analysis of turbidity values showed a steady decrease from upstream to downstream, with turbidity values of >115 NTU and 60–85 NTU in

N. R. Shankar Ram (✉) · K. Mirza
Regional Remote Sensing Centre-North, National Remote Sensing Center, Indian Space Research Organisation, Delhi, India
e-mail: shankarramnr@gmail.com

A. Bhatt
Center for Disaster Management Studies, Jamia Milia Islamia University, New Delhi, India

V. M. Chowdary
Department of Agriculture, Cooperation and Farmers Welfare, Ministry of Agriculture and Farmers Welfare, Government of India, Mahalanobis National Crop Forecast Centre, Delhi, India

C. S. Jha
National Remote Sensing Center, Indian Space Research Organisation, Hyderabad, India

C. Jayaram
Regional Remote Sensing Centre-East, National Remote Sensing Center, Indian Space Research Organisation, Kolkata, India

the upper and lower sections, respectively. The results indicated that remote sensing provides a robust alternative for monitoring surface water turbidity.

Keywords Ganga River · Turbidity · Empirical model · MNDWI · NTU

8.1 Introduction

Climate change has adversely affected the Ganga River basin and its fragile environment in the recent decades. Increased rate of glacier melting and accelerated soil erosion affect the basinwide ecosystem (Ramakrishnan and Rajawat, 2012). Being one of the main water resources for the northern plains of the Indian subcontinent, the Ganga River faces severe challenges due to climate, anthropogenic and environmental changes. Further, increasing population exerts a significant demand for fresh water for consumption and socio-economic development. The key natural factors include contribution from the hydrological, climatic, and geological domains. Changes to the natural hydrology of a region such as the draining of wetlands, the establishment of hydropower units, diversion of river course, etc. disrupt the natural balance in the ecosystem (Du et al. 2010; Manes et al. 2016). Their adverse effects are severe when the water quantities available are low and resources are limited. Human intervention bears serious adversities on the quality of water. In addition to the intensive water usage, activities such as the discharge of industrial, domestic, urban, or other wastes, abundant bottom feeders that stir up bottom sediments or algal growth; the chemical loadings from agricultural lands, either accidental or intentional, result in pollution of water sources (Dietrich et al. 2014; Das 2011, Guttler et al. 2013; Zhou et al. 2006). Thus, to check the rampant deterioration, it is crucial to initially assess the levels of such pollution and further establish a system that monitors its dynamic changes, to plan mitigation or development activities.

Among the various properties of water, turbidity is an important indicator that may be used to investigate river water quality. Turbidity, as a factor of water transparency, provides information about the attenuation of light that is associated with the concentration of total suspended sediments and other impurities present in the water (Devlin et al. 2008; Mishra and Kumar, 2021; Tian et al. 2009). Turbidity can also be understood as a presence of different inorganic and organic materials (particulate or dissolved) in the water. It can also be considered as a measurement of the relative clarity of water, where higher turbidity levels result in increased murkiness of water. Diffusion of light into the water also decreases with the increase of suspended matter, thereby obstructing the amount of light available for photosynthesis. This decreases the extent of vegetative growth, adversely impacting the food chain and also resulting in decreased oxygen levels. Increased turbidity levels also make it difficult for predators that use visual ques to capture their prey (Christian and Sheng, 2003; Devlin et al. 2008).

The particulate matter that ends up in the water bodies originates from sources like soil, plants, animals, industrial effluents, etc. Clay, silt, minute inorganic and organic

matter, dissolved colored organics, algae, plankton, and other microorganisms are examples of such substances. Turbidity is an optical characteristic of water and is a measurement of the quantity of light that is scattered by material in the water when a light passes through the water sample. It is determined by examining water samples on-site or in the lab with the *in-situ* measurements. The higher the intensity of scattered light, the higher the turbidity. It is usually measured in Nephelometric Turbidity Units (NTU), where the instrument measures scattered light from the sample at an angle of 90° from the incoming light (Kitchener et al. 2017). Turbidity measurements of rivers involve the understanding the regime of discharge. It is crucial for the interpretation of measurements of water quality, which include various other parameters viz., flux of contaminants or sediments, suspended sediment, etc. Globally, parameters such as nature of river catchment, its geology, geography as well as climatology also influence the river discharge. In general, water clarity in the river streams tends to be clearer during lean flows, resulting in lower turbidity values, usually less than 10 NTU. During a rainstorm, when water levels are high, most rivers become muddy (brownish) due to suspended sediments from the enhanced terrestrial runoff.

Turbidity is commonly monitored by field measurements and hydrological station observations, which are typically time-intensive and are limited to discrete sites. With the advantage of broad coverage and low cost, remote sensing data provides an alternative way to monitor turbidity at various spatial and temporal scales. The integration of remote sensing data and *in-situ* measurements allows coherent quantification of turbidity changes. Several studies used multispectral and hyper-spectral remote sensing data for turbidity retrieval (Fraser 1998; Frazier and Page, 2000; Ritchie et al. 2003; Kuhn et al. 2019). These studies envisaged multiple algorithms to assess turbidity in riverine waters using different spectral band combinations along with other variables for turbidity assessment. Liu and Wang (2019) developed a reliable turbidity model based on Landsat-8 satellite imagery, while Shen et al. (2021) carried out regression modeling to derive the turbidity from the Yarlung Zangbo River, Southern Tibetan Plateau.

Zhou et al. (2021) generated turbidity maps of the Wuhan region in China, and focused on the turbidity dynamics of this industrial city, for better decision-making and effective water quality management. The relationships of turbidity and metrological and anthropogenic factors were also examined. The study by Kalele (2019) focused on the utilization of satellite spectral reflectance measurements for turbidity retrieval in the Lower Charles River, USA. Similar studies by Allam et al. (2020), Kapalanga et al. (2021), and Pereira et al. (2018) investigated remote sensing-based validation of the satellite-derived values with *in-situ* data over the Ramganga River in the Ganges Basin, Olushandja Dam, north-central Namibia, and Middle Mississippi and Lower Missouri Rivers of the USA, respectively. Specifically, Landsat-8 satellite data have been widely used to estimate water quality parameters. These datasets have been used to examine the spatial and temporal variation of turbidity with the identification of key issues affecting its patterns in El Guajaro Reservoir, Colombia (González-Márquez et al. 2018) and depth in Cam Ranh Bay and the Thuy Trieu Lagoon, Vietnam (Quang et al. 2017). These authors had developed the algorithms to retrieve the turbidity based on the relationship between *in-situ* observations and

the red spectral band of Landsat 8. The study by Surisetty et al. (2018), focused on utilizing Landsat 8 bands, especially Near Infrared (NIR) and Shortwave Infrared (SWIR) to derive turbidity values in the Chilika lagoon.

Thus, various studies were conducted globally to measure the turbidity in major water bodies and river systems using an array of models. The present study comprehensively evaluated some of these algorithms available in literature and aims to identify the most suitable algorithm to effectively retrieve water turbidity across the river Ganga. The specific objectives of the present study include: (1) Assessment of turbidity from satellite data using multiple retrieval algorithms (2) Evaluation of turbidity algorithms using *in-situ* observations (3) Real-time turbidity mapping across various stretches of Ganga River.

8.2 Materials and Methods

8.2.1 Study Area

Ganga River Basin (Fig. 8.1) is the largest river basin in India, covering a total area of 861,404 km^2, comprising the Ganga River and its tributaries. It is marginally greater
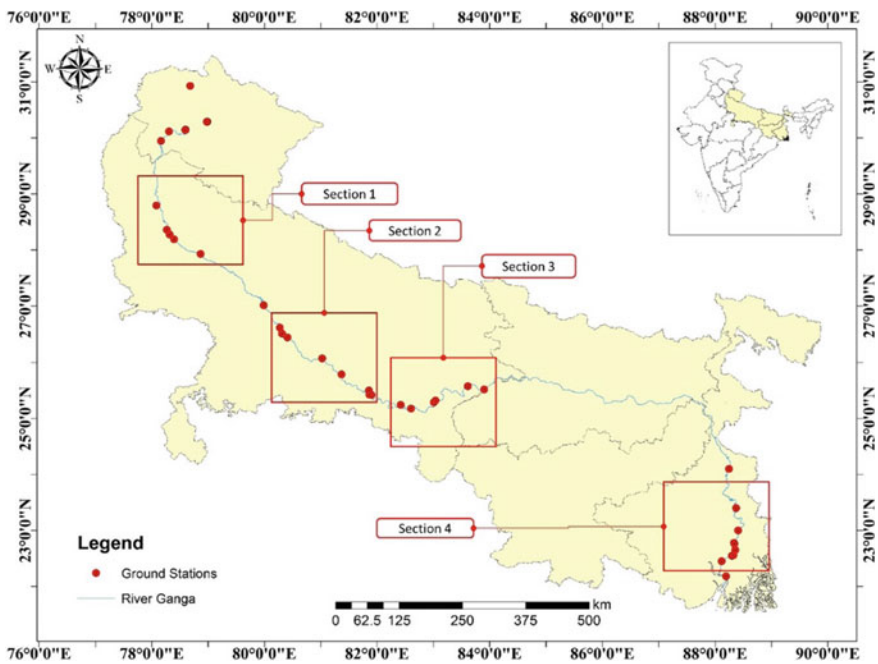

Fig. 8.1 Synoptic view of the study area along with CPCB ground station locations

than a quarter of the total geographical area of the country. This river, considered sacred to billions of Indians, runs along the northern part of India and feeds more than four hundred million people living in the basin area. In total, the Ganga basin is spread in 11 states of the country, namely Bihar, Chhattisgarh, Delhi, Haryana, Himachal Pradesh, Jharkhand, Madhya Pradesh, Rajasthan, Uttar Pradesh, Uttarakhand, and West Bengal. The abundance of water resources, fertile soil, and suitable climatic conditions, across these regions has resulted in an advanced agricultural society with a total cultivated land area of approximately 44 million hectares and a total irrigated area of 23.41 million hectares. It has evolved into one of the most densely inhabited places in the world. The Ganga River has created a basin with extraordinary variations in climatic conditions, altitudes, land use, wildlife, culture, and society. The entire river length was further divided into four river stretches (Fig. 8.1) along the river basin in this study. These stretches were chosen on the basis of availability of *in-situ* datasets and the vicinity of ground station to each other forming a cluster.

8.2.1.1 Climate

The average maximum and minimum temperature across the basin fall in the of range of 30.3 °C–21.5 °C in summer to 21.1 °C–6.4 °C in winter, respectively. The pre-monsoon season (March–May) experiences the hottest temperatures in the basin with an average temperature of ~31.4 °C. The month of January is the coldest across the whole basin. The annual precipitation across the basin is nearly 1000 mm. The monsoon season witnesses the highest amount of rainfall (nearly 84% of the annual total). Of the remainder, 7, 5, and 4% fall during the pre-monsoon, post-monsoon, and winter seasons with some differences in precipitation between the upper and lower Ganges basins. Generally, peak flows occur when melting of snow runoff is reinforced by monsoon rains. The Ganges receives snow-melt from southern flaks of Tibet as well as the Himalayas from the periods from April, extending till June, and subsequently, the flow rate of the river commences to decrease when the July monsoon commences.

8.2.1.2 Topography and Soil Characteristics

The Gangetic plains are generally distributed into the Upper, the Middle, and the Lower Ganga plains, respectively. Approximately 40% of the total Ganga basin area falls under the elevation of 50–200 m. It is confined by the mighty Himalayas in the north, the Vindhyas range and Chotanagpur plateau in the south, the Aravalli range across the west, and the Brahmaputra ridge in the east. The river basin comprises an extensive variety of soils. While the high Himalayan soils in the north face continuous erosion, the Gangetic plain provides a huge depositional platform forming a wide valley plain, where some soils are highly prone to erosion. The montane and alluvial soils cover nearly 60% of the total basin area. Of the remaining area, red soils (12% area) are highly erodible, yellow and red soils, mixed black and red soils (8% area)

have moderate erodibility, and medium and deep black soils (14% area) have low erodibility. Lateritic soils and shallow black soils that cover 6% of the basin area have very low erodibility.

8.2.2 In-Situ and Satellite Datasets Used in the Study

The present study investigated the agreement of satellite-based retrieval of turbidity with water quality information collected from the Central Pollution Control Board [CPCB] for the period 2013–2016 (CPCB 2008). A total of 40 ground stations datasets spanning across the study region, i.e., situated between Indian state of Uttarakhand (headwaters) to Sundarbans Delta, West Bengal (mouth of the river) were used in the analysis. The datasets contained turbidity information from *in-situ* instruments placed along the banks of the river. In the present analysis, 17 ground station datasets were selected based on the factors such as concurrent availability with satellite pass and data quality (Fig. 8.1).

Satellite-based imagery from the Landsat-8 satellite in the Landsat series satellites was used in the present study. The satellite payload has two scientific instruments onboard- the Operational Land Imager (OLI) and the Thermal Infrared Sensor (TIRS). These sensors deliver periodic coverage of the landmass with a spatial resolution of 30 m across the NIR, SWIR, and visible bands; 100 m across the Thermal band and 15 m across the Panchromatic band (Table 8.1). An inventory of all available satellite datasets between the year 2013–2016 was generated and concurrent dates

Table 8.1 Spectral bands and resolutions of Landsat 8

Bands	Wavelength (nm)	Type	Spatial resolution (m)
1	430–450	Coastal aerosol	30
2	450–510	Blue	30
3	530–590	Green	30
4	640–670	Red	30
5	850–880	Near Infrared (NIR)	30
6	1570–1650	SWIR 1	30
7	2110–2290	SWIR 2	30
8	500–680	Panchromatic	15
9	1360–1380	Cirrus	30
10	10,600–11,190	Thermal Infrared (TIRS) 1	100
11	11,500–12,510	Thermal Infrared (TIRS) 2	100

Source Hansen and Loveland (2012)

that correspond to CPCB ground station measurement for a satellite overpass were identified. These datasets have been downloaded from the USGS website (Hansen and Loveland 2012) and further processed in this study.

8.2.3 Methodology

Landsat-8 images for the four selected stretches were obtained and further processed by following the methodology as discussed subsequently.

8.2.3.1 Generation of River Mask

The computational intensity to process the satellite datasets was reduced by subsetting the datasets into pixels with only the river course. The Modified Normalized Difference Water Index (MNDWI), which enhances open water features while sufficiently suppressing and removing the built-up land noise as well as soil/vegetation noise was used in the present study (Xu 2006). The index is derived from the modification of the Normalized Difference Water Index (NDWI) (Gao 1996; McFeeters, 1996), by substituting the middle infrared band with the Near Infrared (NIR) band used in the NDWI. The NDWI extracted water area is overestimated as the water mask obtained from satellite imagery is usually mixed up with built-up land noise. Hence, MNDWI, helps in contracting and even eliminating the noise of built-up land and is more suitable for extraction and enhancement of water features with a built-up dominated land area in background. The formula used to compute the MNDWI can be computed as follows:

$$MNDWI = (Green - SWIR)/(Green + SWIR)$$

Where "Green" is the green band and "SWIR" is the Short Wave Infrared band. The water pixels are extracted from the generated MNDWI values by applying a threshold at 0.

8.2.3.2 Extraction of Surface Reflectance for River Mask

The satellite imagery from the four identified river sections was clipped with the water vector polygon. Pixel values from bands 2, 3, 4, and 5 of the clipped satellite imageries are converted to surface reflectance values using a multiplicative factor (0.0000275) as given in the Landsat 8 OLI/TIRS Collection 2 Level 2 Data Format Control Book (USGS 2020).

Table 8.2 Turbidity models evaluated across the river stretch

S. No.	Retrieval model	References
1	$T = -74.26 * B2 - 14.84 * B3 + 267.45 * B4 - 126.89 * B5 + 4.21$ B2 = Band 2, B3 = Band 3, B4 = Band 4, B5 = Band 5	Liu and Wang (2019)
2	$T = -344.784 * B2 + 398.817 * B3 + 1.045$ B2 = Band 2, B3 = Band 3	Kalele (2019)
3	$T = -138.2 - 1718 * (B4/B3) + 695.1 * e(B4/B3)$ e = exponential, B3 = Band 3, B4 = Band 4	Pereira et al. (2018)
4	$T = 380.32 * (B4) - 1.7826$ B4 = Band 4	Quang et al. (2017)
5	Turbidity = 10.26 * (B4 + B5) − 0.18359 B4 = Band 4, B5 = Band 5	González-Márquez et al. (2018)
6	$T = 15.31856 - 956.806 * (B2) - 747.376 * (B3) + 1742.455 * (B4) + 165.173(B5)$ B2 = Band 2, B3 = Band 3, B4 = Band 4, B5 = Band 5	Kapalanga et al. (2021)
7	$T = 3.896 - 4.186 * (\text{Band 2/Band 3})$	Allam et al (2020)
8	$T = 23.09 * (r - 0.233/1.28 - r)$ r = broadband reflectance ratio of B4/B3	Surisetty et al. (2018)
9	$T = (1 - \varepsilon) * 2.1170 * (\text{red band}) * 2.4880 + \varepsilon * 2.4354 * (\text{NIR}) * 2.5673$ $\varepsilon = (\text{NIR band} - 0.028)/0.005$	Zhou et al. (2021)
10	$T = 253.884 + (-558.206 * X) + (0 * X2) + (399.496 * X3)$ X = Band 4/Band 3	Li et al (2015)

8.2.3.3 Turbidity Retrieval Algorithms

The widely used strategy to compute turbidity is to establish the relationships between turbidity and image reflectance based on the calibration of *in-situ* measurements from water samples. In this study, we used multiple models from literature to extract the best-suited turbidity model for the Ganga River. Table 8.2 catalogs the 10 turbidity models evaluated in the present study. Each algorithm was implemented over the river sections and the resulting turbidity values were compiled. The results were further evaluated for consistency in their range of values in comparison to *in-situ* datasets and four models were identified.

8.2.3.4 Performance Evaluation of Turbidity Models

Subsequent to obtaining the outputs of all the algorithms, four algorithms were shortlisted based on their value ranges for the validation process. The pixel values

of coordinates falling over the *in-situ* ground stations and model-based extracted turbidity datasets were acquired for all four algorithms, following the nearest neighborhood criteria with the *in-situ* location. The relative performance of these models is evaluated based on the Root Mean Square Error (RMSE) calculation. RMSE is the residual's standard deviation (prediction errors). Residuals measure the distance of the regression line from the data point, showing the spread. This error metric is commonly used in climatology, forecasting, and regression analysis to verify experimental results. The formula to compute RMSE is as follows:

$$\text{RMSE} = \sqrt{\frac{\sum_{i=0}^{N} \left(x_i - \hat{x}_i\right)^2}{N}}$$

N = No. of datasets
x_i = *in-situ* based value
$\hat{x}_i$ = Model-based value.

Subsequent to the validation of the four shortlisted models of turbidity, the most suitable algorithm is selected based on the lowest deviation in the values between *in-situ* data and observed data.

8.2.3.5 Real-Time Turbidity Mapping Across the Ganga River

Cloud-free satellite datasets across the study area were acquired to compute the turbidity across the river. These maps may serve as guiding tools to identify turbidity levels across various stretches of the study area.

8.3 Result and Discussion

Remote sensing and GIS-based technologies were used to retrieve the turbidity of Ganga River. Satellite imagery of the study period from 2013 to 2016 was downloaded and the coordinates of the respective ground stations along with dataset's path and row numbers of the satellite imagery, along with their corresponding dates, are presented in Table 8.3. The description of various intermediate steps and results that were carried across these datasets are as described below.

8.3.1 Extraction of Water Pixels and Generation of River Mask

The MNDWI algorithm was applied onto the Landsat satellite across the identified river stretches. Figure 8.2a, b, show the False-color composite and the MNDWI

Table 8.3 Inventory of satellite data availability corresponding to *in-situ* data with their date of availability

| Year	Date	Ground station	Coordinates (latitude, longitude)	Path, row	Landsat 8 Datasets (LC08_L2SP_…)
Section 1					
2013	22-May	G1	28.2731, 78.3182	145, 41	…145041_20130522_20200913_02_T1
2014	17-Nov	G2	28.1897, 78.3959	145, 41	…145041_20141117_20200910_02_T1
Section 2					
2014	09-Apr	G3	25.4192, 81.9005	143, 42	…143042_20140409_20200911_02_T1
2015	23-Feb	G4	25.5023, 81.8554	143, 42	…143042_20150223_20200909_02_T1
		G5	25.4192, 81.9005	143, 42	…143042_20150223_20200909_02_T1
2016	01-Jun	G6	25.4266, 81.8639	143, 42	…143042_20160601_20200906_02_T1
Section 3					
2014	09-Apr	G7	25.244, 82.4183	143, 42	…143042_20140409_20200911_02_T1
2016	25-May	G8	25.1771, 82.6022	142, 43	…142043_20160525_20200906_02_T1
		G9	25.244, 82.4183	142, 43	…142043_20160525_20200906_02_T1
	03-Feb	G10	25.2894, 83.0064	142, 42	…142042_20160203_20200907_02_T1
		G11	25.3199, 83.0366	142, 42	…142042_20160203_20200907_02_T1
Section 4					
2014	02-Dec	G12	22.4535, 88.1153	138, 44	…138044_20141202_20200910_02_T1
	08-May	G13	22.4535, 88.1153	138, 44	…138044_20140508_20200911_02_T1
2015	12-May	G14	23.4001, 88.3734	138, 44	…138044_20151205_20200908_02_T1
		G15	23.0008, 88.4086	138, 44	…138044_20151205_20200908_02_T1
	02-Oct	G16	22.5497, 88.2961	138, 44	…138044_20151002_20200908_02_T1
2016	07-Dec	G17	22.5497, 88.2961	138, 44	…138044_20161207_20200905_02_T1
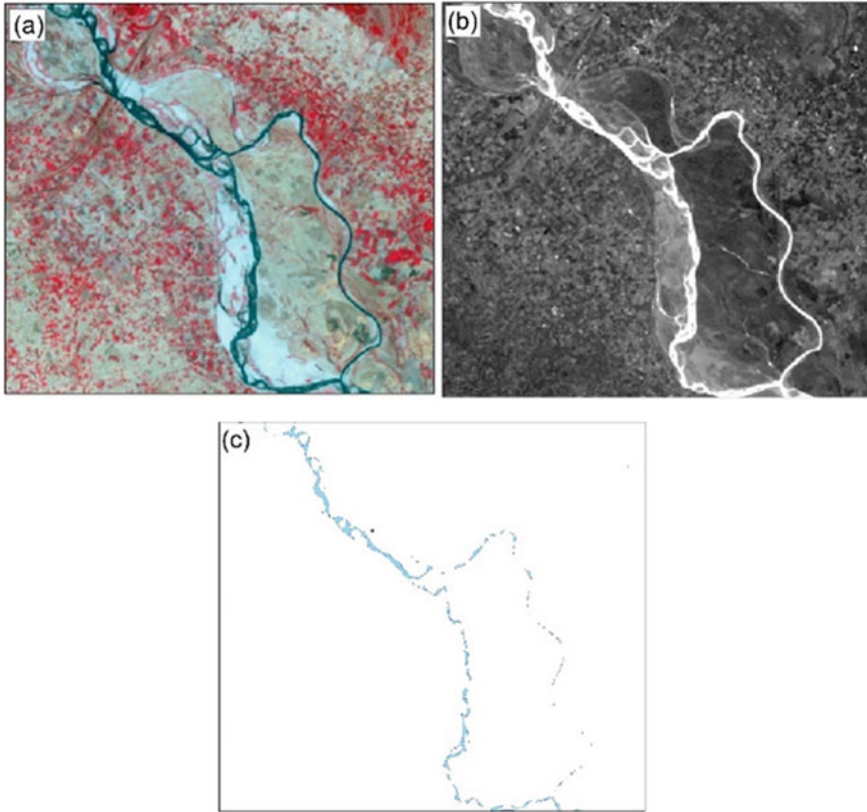
Fig. 8.2 Sample section of the river showing **a** FCC imagery, **b** modified normalized difference water index and **c** river mask

output, respectively across a sample section of the river. The water pixels are extracted by the application of threshold value of 0 onto the MNDWI output. Subsequently, these pixels were converted to vector polygon so as to generate the river mask (Fig. 8.2c).

8.3.2   Estimation of Turbidity Using Multiple Turbidity Retrieval Algorithms

The satellite datasets were clipped and the surface reflectance values were computed for these datasets across the study region as defined in Sect. 8.2.3. The value ranges of all these models were computed and four models with their values lying within the range of values in the *in-situ* datasets were shortlisted. The algorithms from Liu and Wang (2019) (Sr. No. 1), Kalele (2019) (Sr. No. 2), Quang et al. (2017) (Sr. No.

Table 8.4 Shortlisted models for turbidity extraction

Model No	Selected model	References
A	$T = -74.26 * B2 - 14.84 * B3 + 267.45 * B4 - 126.89 * B5 + 4.21$ B2 = Band 2, B3 = Band 3, B4 = Band 4, B5 = Band 5	Liu and Wang (2019)
B	$T = -344.784 * B2 + 398.817 * B3 + 1.045$ B2 = Band 2, B3 = Band 3	Kalele (2019)
C	$T = 380.32 * (B4) - 1.7826$ B4 = Band 4	Quang et al. (2017)
D	$T = 253.884 + (-558.206 * X) + (0 * X2) + (399.496 * X3)$ X = Band 4/Band 3	Li et al (2015)

4), and Li et al. (2015) (Sr. No.10) were taken as Models A, B, C, and D, respectively (Table 8.4).

8.3.3 Estimation of Turbidity Across River Sections Using Different Turbidity Models

The shortlisted turbidity models (Models A, B, C & D) were applied to each section of the river. The values of turbidity across the models over the river Section 1 are shown in Fig. 8.3. Here, the computed turbidity values indicated values ranging from 7 to 39 NTU and 26 NTU to 53 NTU for Model A and Model B, respectively. Model B showed an average turbidity higher than the Model A estimated value. The turbidity estimates from Model C are observed from 99 to 181 NTU which is the highest among all the other algorithms. Although there were only few values greater than 170 NTU, the average values were well over 120 NTU. Turbidity values from Model D also indicated high values with NTU ranging from 65 to 171 NTU.

Figure 8.4 depicts the computed turbidity for various models across Sect. 2 of the study area. The turbidity values ranged from 6 to 38 NTU. The distribution of turbidity was seen to vary with lower values in the upper part of the river and increasing toward the downstream region. Models A and B showed values between 38 and 49 NTU, respectively. Model B showed not only higher turbidity in comparison to Model A, but it also showed greater number of stretches with high values. The output of Model C and D showed turbidity values from 87 to 170 NTU and from 47 to 187 NTU, respectively. Although Model D had the highest maximum value of computed turbidity, Model C showed the highest average value. Low to moderate values of turbidity was observed in the upper part and higher values were computed in the lower part of the river.

The distribution of turbidity across different turbidity models were shown in Fig. 8.5. The output of Model A showed that the turbidity values ranged from 03 to 38 NTU. Few regions where minor tributaries converge showed high turbidity values.
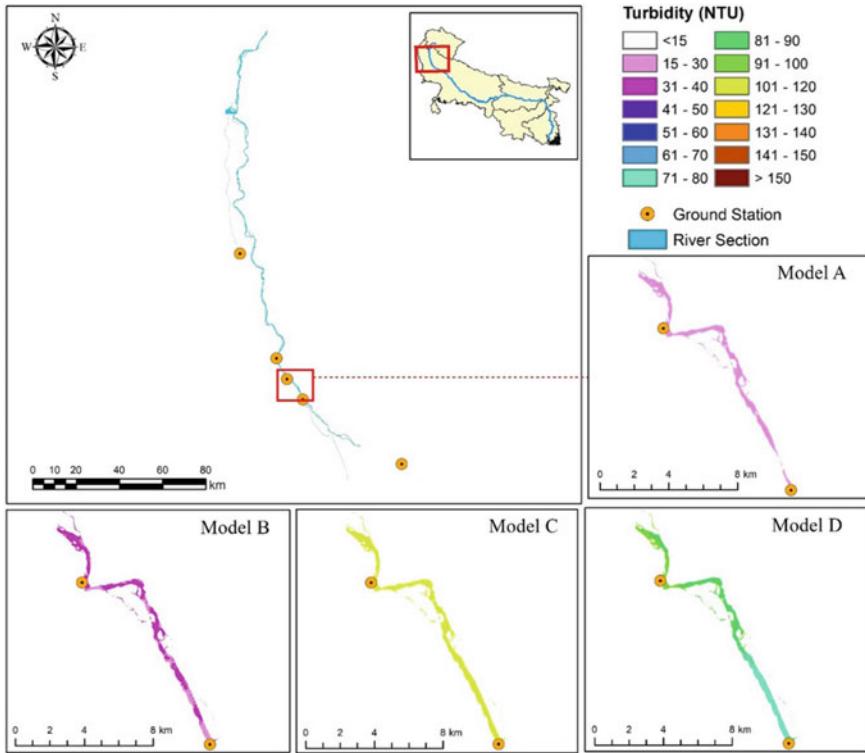
Fig. 8.3 Spatial distribution of turbidity for Models A, B, C & D across Section 1

The turbidity output of Model B (18 NTU to 48 NTU) showed rather low values along the upper and middle part of the river section with higher values in the lower part after the tributaries converge. Model C indicated values ranging from 83 to 149 NTU and 47 NTU to 153 NTU, respectively. They showed the gradual increase in values toward the downstream regions.

Figure 8.6 depicts the turbidity outputs for Models A, B, C, and D across the lowest section (Section 4) of the study region. The output of Model A depicted values that ranged from negligible to 42 NTU. The pixels values for turbidity ranged from low to moderate from the upstream toward downstream regions. The output of Model B (7–70 NTU), showed patterns of the turbidity to be higher in the middle regions of the river while moderate toward the upper and lower reaches of the river. Models C (turbidity between 72 and 248 NTU) showed similar patterns. There were few regions of the river which showed values that exceeded 200 NTU. Model D (turbidity between 16 and 138 NTU) showed low values in the upstream and downstream regions of the river and regions in the middle showed moderate to high turbidity values.
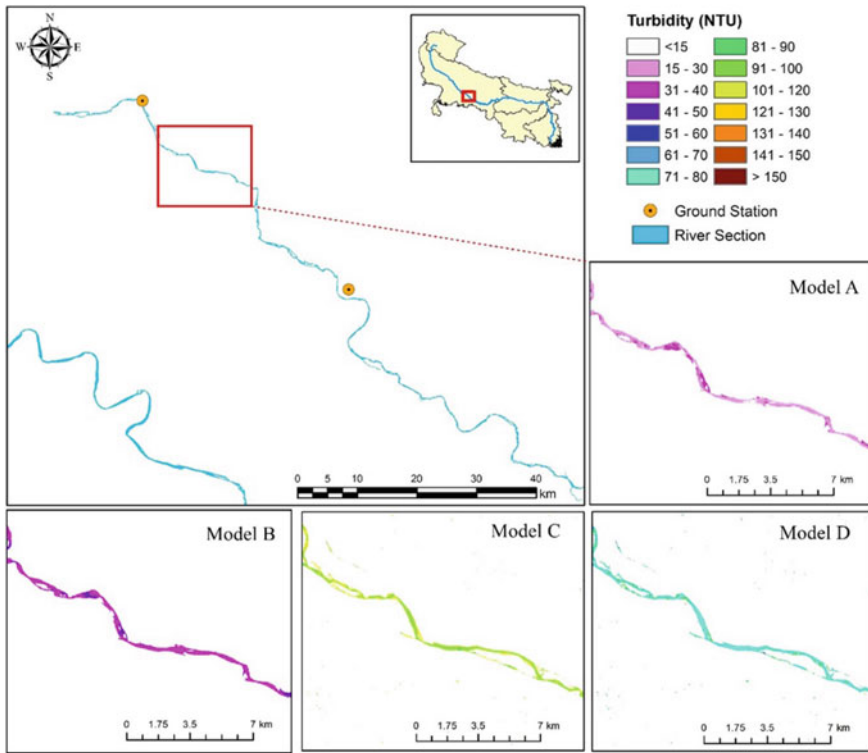
Fig. 8.4 Spatial distribution of turbidity for Models A, B, C & D across Section 2

8.3.4 Evaluation of Turbidity Retrieval Models Using In-Situ Observations

The model outputs for pixels near the spatial vicinity of *in-situ* observation sites were extracted considering the dates and satellite data availability. To extract the model that most accurately represents the *in-situ* datasets, the RMSE matric was computed across various sections of the river. Tables 8.5, 8.6, 8.7 and 8.8 show the RMSE values across various sections of the study area. It was observed that Sections 2, 3, and 4 were best represented by Model D (Li et al. 2015) with the RMSE values of 8.27, 24.18, and 62.65, respectively which indicated that it was a moderately suitable algorithm among these river sections. On the contrary, Model B (Kalele 2019) showed the lowest RMSE error (12.1) for Section 1 of the study area, indicating better performance. In the present study, since Model D depicted the least RMSE value across three different sections, it was selected as the most suitable algorithm among all the other algorithms for estimation of turbidity across the Ganga River.
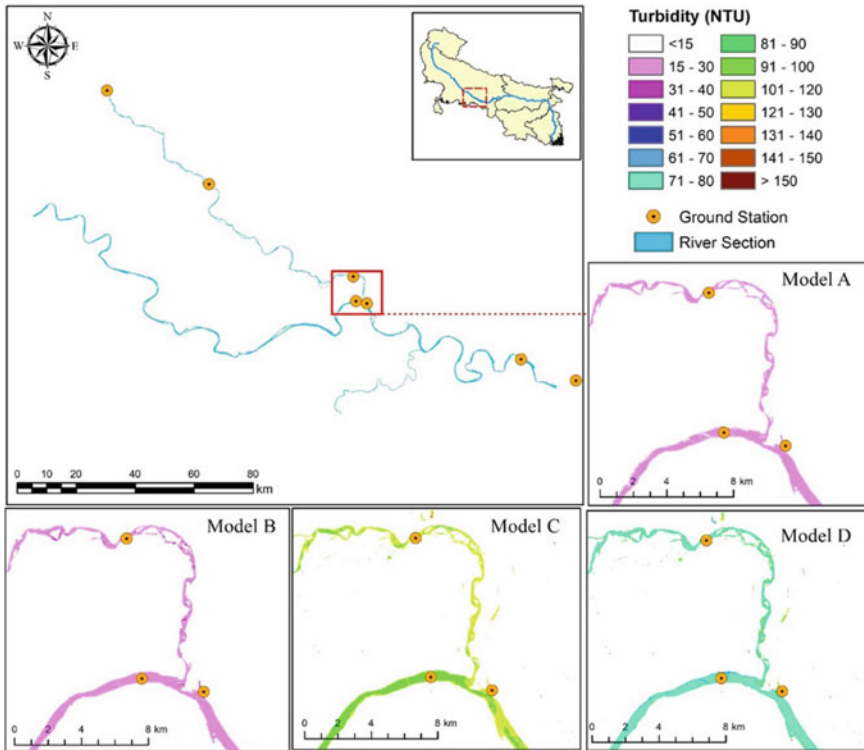
Fig. 8.5 Spatial distribution of turbidity for Models A, B, C & D across Section 3

8.3.5   Real-Time Turbidity Mapping Through the Best Performing Model

Satellite datasets of 13-July-2021 were acquired and the water turbidity across the study area was computed using the most suitable turbidity retrieval algorithm as proposed by Li et al. (2015) (Model D) (Fig. 8.7). The upper reaches of the river exhibited higher turbidity (>115 NTU) values in comparison to the downstream sections (60-85 NTU) after the confluence with its tributaries. During its passage across the middle reaches, the river confluences with many of its tributaries, creating turbid waters. The reduction of turbidity values toward its lower reaches may be attributed to the widening and slowing down of the course of the river, allowing for the settling of particulate matter, thereby reducing water turbidity in the downstream sections. The turbidity values retrieved in the present approach may be operationalized to continually monitor the water quality across the river.
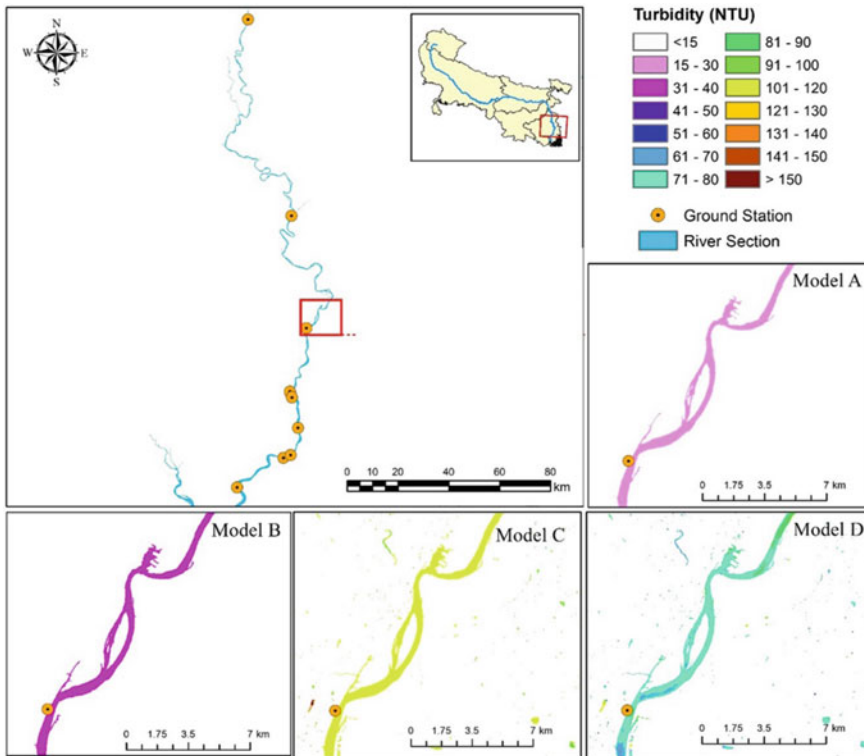
Fig. 8.6 Spatial distribution of turbidity for Models A, B, C & D across Section 4

8.4 Conclusions

Water quality is influenced by a wide range of human and natural factors. Turbidity is an important indicator of water quality and the hydrological conditions of rivers. With the advantage of synoptic coverage and low costs, satellite data and remote sensing techniques have opened up new avenues and provided alternative ways to monitor turbidity at various spatial and temporal scales. The present study investigated the turbidity retrieval from satellite datasets using various retrieval models available across literature. The study further envisaged to identify the most suitable algorithm, that best represented the *in-situ* observations across different sections over the Ganga River. The study indicated that model proposed by Li et al. (2015), best represented the turbidity concentration in the river waters of the Ganga. However, the model was unable to represent the *in-situ* turbidity values across the upstream sections of the river satisfactorily. Thus, a single model may not be adequate to completely model the complete extent of large river systems such as the Ganga. Thus, there is scope for novel models, which may quantitatively best represent different sections of the river course, with is varying agro-climatic and morphological characteristics.

Table 8.5 Relative performance of turbidity model across *in-situ* observations for Section 1

Year	Date	Station no	Observed values	Algorithms							
				Model A		Model B		Model C		Model D	
				Predicted value	RMSE	Predicted value	RMSE	Predicted value	RMSE	Predicted value	RMSE
2013	22/05	G1	42	25	12.10	34	5.65	104	59.07	76	24.30
2014	17/11	G2	30	28		30		86		35	

Table 8.6 Relative performance of turbidity model across *in-situ* observations for Section 2

Year	Date	Station no	Observed Values	Algorithms										
				Model A		Model B		Model C		Model D	
				Predicted value	RMSE	Predicted value	RMSE	Predicted value	RMSE	Predicted value	RMSE
2014	09/04	G3	60	24	35.27	32	27.02	91	32.41	66	8.27
2015	23/02	G4	68	24		33		90		68	
		G5	59	26		34		85		63	
2016	01/06	G6	60	25		36		102		71	

Table 8.7 Relative performance of turbidity model across *in-situ* observations for Section 3

Year	Date	Station no	Observed values	Algorithms							
				Model A		Model B		Model C		Model D	
				Predicted value	RMSE	Predicted value	RMSE	Predicted value	RMSE	Predicted value	RMSE
2014	09/04	G7	72	26	57.14	32	50.12	124	46.65	105	24.18
2016	25/05	G8	108	23		34		108		106	
		G9	108	25		34		109		108	
	03/02	G10	20	20		22		91		54	
		G11	30	20		27		86		56	

Table 8.8 Relative performance of turbidity model across *in-situ* observations for Section 4

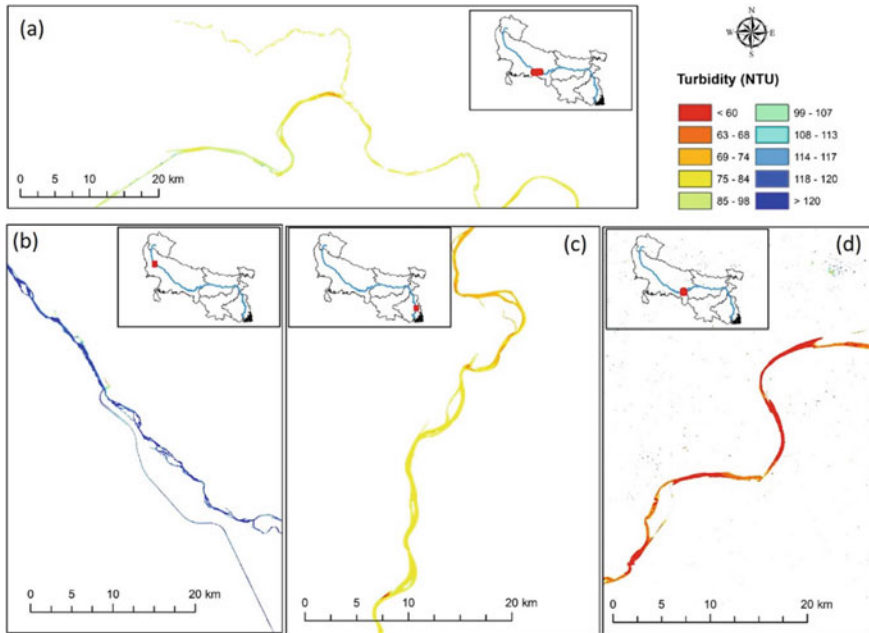| Year	Date	Station no	Observed values	Algorithms							
				Model A		Model B		Model C		Model D	
				Predicted value	RMSE	Predicted value	RMSE	Predicted value	RMSE	Predicted value	RMSE
2014	02/12	G12	27	27	108.38	27	103.45	101	67.03	64	62.65
	08/05	G13	51	26		40		100		52	
2015	12/05	G14	186	23		37		126		89	
		G15	99	27		40		100		99	
	02/10	G16	32	23		32		92		34	
2016	07/12	G17	226	31		30		117		113	

Fig. 8.7 Spatial distribution of turbidity across a) middle (moderate turbidity), b) upper (high turbidity), c) lower (moderate turbidity) and d) middle (high turbidity) river sections using turbidity Model D

References

Allam M, Khan MYA, Meng Q (2020) Retrieval of turbidity on a spatio-temporal scale using Landsat 8 SR: a case study of the Ramganga River in the Ganges Basin, India. Appl Sci 10(11):3702

Christian D, Peter Sheng Y (2003) Relative influence of various water quality parameters on light attenuation in Indian River Lagoon. Estuarine Coast Shelf Sci 57(5–6):961–971

CPCB (2008) Guidelines for water quality monitoring (2007–2008). Central Pollution Control Board CPCB. Ministry of Environment. For. MINARS/27/2007-08. 06-15

Das S (2011) Cleaning of the Ganga. J Geol Soc India 78(2):124–130

Devlin MJ, Barry J, Mills DK, Gowen RJ, Foden J, Sivyer D, Tett P (2008) Relationships between suspended particulate material, light attenuation and Secchi depth in UK marine waters. Estuar Coast Shelf Sci 79(3):429–439

Dietrich AM, Phetxumphou K, Gallagher DL (2014) Systematic tracking, visualizing, and interpreting of consumer feedback for drinking water quality. Water Res 66:63–74

Du N, Ottens H, Sliuzas R (2010) Spatial impact of urban expansion on surface water bodies—a case study of Wuhan, China. Landsc Urban Plan 94(3–4):175–185

Fraser RN (1998) Multispectral remote sensing of turbidity among Nebraska Sand Hills lakes. Int J Remote Sens 19(15):3011–3016

Frazier PS, Page KJ (2000) Water body detection and delineation with Landsat TM data. Photogramm Eng Remote Sens 66(12):1461–1468

Gao B-C (1996) NDWI—A normalized difference water index for remote sensing of vegetation liquid water from space. Remote Sens Environ 58(3):257–266

González-Márquez LC, Torres-Bejarano FM, Torregroza-Espinosa AC, Hansen-Rodríguez IR, Rodríguez-Gallegos HB (2018) Use of LANDSAT 8 images for depth and water quality assessment of El Guájaro reservoir, Colombia. J South Am Earth Sci 82:231–238

Güttler FN, Niculescu S, Gohin F (2013) Turbidity retrieval and monitoring of Danube Delta waters using multi-sensor optical remote sensing data: an integrated view from the delta plain lakes to the western–northwestern Black Sea coastal zone. Remote Sens Environ 132:86–101

Hansen MC, Loveland TR (2012) A review of large area monitoring of land cover change using Landsat data. Remote Sens Environ 122:66–74

Kalele AS (2019) Estimation and mapping of turbidity in the lower Charles River Using Landsat 8 OLI satellite imagery. PhD diss., Northeastern University, 2019

Kapalanga TS, Hoko Z, Gumindoga W, Chikwiramakomo L (2021) Remote-sensing-based algorithms for water quality monitoring in Olushandja Dam, north-central Namibia. Water Supply 21(5):1878–1894

Kitchener BGB, Wainwright J, Parsons AJ (2017) A review of the principles of turbidity measurement. Progress Phys Geogr 41(5):620–642

Kuhn C, de Matos Valerio A, Ward N, Loken L, Sawakuchi HO, Kampel M, Richey J et al (2019) Performance of Landsat-8 and Sentinel-2 surface reflectance products for river remote sensing retrievals of chlorophyll-a and turbidity. Remote Sens Environ 224:104–118

Li H, Li Y, Shen W, Li Y, Lin J, Xiaoyu L, Xia X, Jiang J (2015) Elevation-dependent vegetation greening of the Yarlung Zangbo River basin in the southern Tibetan Plateau, 1999–2013. Remote Sens 7(12):16672–16687

Liu L-W, Wang Y-M (2019) Modelling reservoir turbidity using Landsat 8 satellite imagery by gene expression programming. Water 11(7):1479

Manes F, Marando F, Capotorti G, Blasi C, Salvatori E, Fusaro L, Ciancarella L et al (2016) Regulating ecosystem services of forests in ten Italian metropolitan cities: air quality improvement by PM10 and O3 removal. Ecol Indicators 67:425–440

McFeeters SK (1996) The use of the Normalized Difference Water Index (NDWI) in the delineation of open water features. Int J Remote Sens 17(7):1425–1432

Mishra S, Kumar A (2021) Estimation of physicochemical characteristics and associated metal contamination risk in the Narmada River, India. Environ Eng Res 26(1)

Pereira LSF, Andes LC, Cox AL, Ghulam A (2018) Measuring suspended-sediment concentration and turbidity in the middle Mississippi and lower Missouri rivers using landsat data. JAWRA J Am Water Resour Assoc 54(2):440–450

Quang NH, Sasaki J, Higa H, Huan NH (2017) Spatiotemporal variation of turbidity based on landsat 8 oli in cam ranh bay and thuy trieu lagoon, vietnam. Water 9(8):570

Ramakrishnan R, Rajawat AS (2012) Simulation of suspended sediment transport initialized with satellite derived suspended sediment concentrations. J Earth Syst Sci 121(5):1201–1213

Ritchie JC, Zimba PV, Everitt JH (2003) Remote sensing techniques to assess water quality. Photogramm Eng Remote Sens 69(6):695–704

Shen M, Wang S, Li Y, Tang M, Ma Y (2021) Pattern of turbidity change in the middle reaches of the Yarlung Zangbo River, Southern Tibetan Plateau, from 2007 to 2017. Remote Sens 13(2):182

Surisetty VVAK, Sahay A, Ramakrishnan R, Samal RN, Rajawat AS (2018) Improved turbidity estimates in complex inland waters using combined NIR–SWIR atmospheric correction approach for Landsat 8 OLI data. Int J Remote Sens 39(21):7463–7482

Tian T, Merico A, Jian S, Staneva J, Wiltshire K, Wirtz K (2009) Importance of resuspended sediment dynamics for the phytoplankton spring bloom in a coastal marine ecosystem. J Sea Res 62(4):214–228

USGS/EROS (2020) Landsat 8–9 Operational Land Imager (OLI)-Thermal Infrared Sensor (TIRS) Collection 2 level 2 (L2) Data Format Control Book (DFCB), Department of the interior, U.S. Geological survey

Xu H (2006) Modification of normalised difference water index (NDWI) to enhance open water features in remotely sensed imagery. Int J Remote Sens 27(14):3025–3033

Zhou Q, Wang J, Tian L, Feng L, Li J, Xing Q (2021) Remotely sensed water turbidity dynamics and its potential driving factors in Wuhan, an urbanizing city of China. J Hydrol 593:125893
Zhou W, Wang S, Zhou Y, Troy A (2006) Mapping the concentrations of total suspended matter in Lake Taihu, China, using Landsat-5 TM data. Int J Remote Sens 27(6):1177–1191